Thermodynamic and Structural Insights into Nanocomposites Engineering by Comparing Two Materials Assembly Techniques for Graphene

Jian Zhu,[†] Huanan Zhang,[†] and Nicholas A. Kotov[†,‡,§,⊥,*]

[†]Department of Chemical Engineering, [‡]Department of Materials Science and Engineering, [§]Department of Biomedical Engineering, and [⊥]BioInterface Institute, University of Michigan, Ann Arbor, Michigan 48109, United States

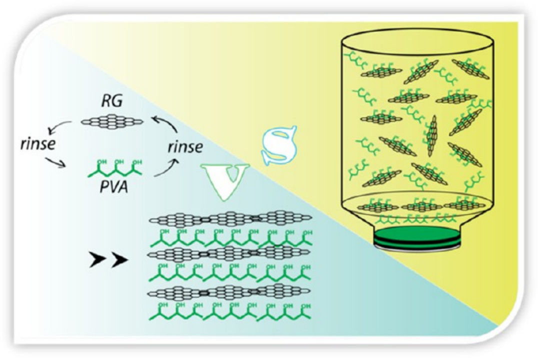

ABSTRACT Materials assembled by layer-by-layer (LBL) assembly and vacuum-assisted flocculation (VAF) have similarities, but a systematic study of their comparative advantages and disadvantages is missing. Such a study is needed from both practical and fundamental perspectives aiming at a better understanding of structure−property relationships of nanocomposites and purposeful engineering of materials with unique properties. Layered composites from polyvinyl alcohol (PVA) and reduced graphene (RG) are made by both techniques. We comparatively evaluate their structure, mechanical, and electrical properties. LBL and VAF composites demonstrate clear differences at atomic and nanoscale structural levels but reveal similarities in micrometer and submicrometer organization. Epitaxial crystallization and suppression of phase transition temperatures are more pronounced for PVA in LBL than for VAF composites. Mechanical properties are virtually identical for both assemblies at high RG contents. We conclude that mechanical properties in layered RG assemblies are largely determined by the thermodynamic state of PVA at the polymer/nanosheet interface rather than the nanometer scale differences in RG packing. High and nearly identical values of toughness for LBL and VAF composites reaching 6.1 MJ/m^3 observed for thermodynamically optimal composition confirm this conclusion. Their toughness is the highest among all other layered assemblies from RG, cellulose, clay, *etc*. Electrical conductivity, however, is more than 10× higher for LBL than for VAF composites for the same RG contents. Electrical properties are largely determined by the tunneling barrier between RG sheets and therefore strongly dependent on atomic/nanoscale organization. These findings open the door for application-oriented methods of materials engineering using both types of layered assemblies.

KEYWORDS: materials design · graphene · polyvinyl alcohol · PVA · strength · toughness · conductivity · layer-by-layer assembly · LBL · vacuum-assisted flocculation · VAF · adsorption thermodynamics

High-performance nanocomposites require high concentrations of nanomaterial phase (inorganic component or filler) with a carefully engineered interface with the polymer matrix. Tight control over the structure at different scales is the key to ensure a material's uniformity and to minimize the contribution of defects of different natures. At the same time, the influence of structural features found at different scales—atomic, nanometer, submicrometer, micrometer, *etc.*—on different properties is only partially understood. Greater clarity in the multiscale structure−property relationships is needed in order to conceptualize material engineering. In particular, multiscale engineering of materials is needed to identify an unusual combination of dissimilar properties. Many technological bottlenecks[1−3] require a set of properties that can be described as "mechanics+" combinations that define the targets for materials performance as parameter pairs, triplets, *etc.*, linking mechanical, electrical, optical, and other properties into figures of merit or graphs.[4]

Among new methods developed for such materials are layer-by-layer (LBL) assembly and vacuum-assisted flocculation (VAF). They stand out among others by their demonstrated success with unusual "mechanics+" combinations for a variety

* Address correspondence to kotov@umich.edu.

Received for review December 12, 2012 and accepted May 9, 2013.

10.1021/nn400972t

of nanoscale components including clay,[1,5] cellulose,[6,7] carbon nanotubes (CNTs),[4,8] and lately graphene and its derivatives.[9−13] Materials produced by LBL and VAF have apparent similarities and can potentially be used for the same applications. A systematic study of their advantages and disadvantages is missing, however, despite being much needed when selecting one or the other technique for high-performance materials. In addition, this study could enlighten us as to the helpful concepts for multiscale materials engineering of advanced composites.

On the basis of the large body of literature data,[4,10,14,15] one could expect that LBL composites should have better nanoscale organization and uniformity than VAF-made materials due to the higher accuracy of the step-by-step deposition with typically one nanoscale layer at a time.[16,17] VAF-made materials are expected to have virtually the same functional properties, while the time needed to assemble similar laminated structures[10,18−20] should be much shorter. The objective of this work is to make such a comparison with respect to properties and correlate it with structure differences. The VAF *vs* LBL comparison allows not only drawing conclusions regarding these particular composites but also advancing materials engineering as a research field, as this comparison is able to build a framework for the correlation between specific properties and structural features and guide future materials preparation with justifiable *a priori* expectations of properties, which often strongly deviate—quantitatively and qualitatively—from predictions made by any frequently used classical models.

The choice of components to obtain an adequate LBL *vs* VAF comparison needs to be carefully contemplated. One should consider the possibility (1) to investigate multiple "mechanics+" performance characteristics and (2) to prepare both LBL and VAF composites from identical components under identical conditions. It was, in fact, more difficult than one could expect. Reduced graphene (RG) and polyvinyl alcohol (PVA) provide a model system suitable for this study. LBL *vs* VAF comparison for PVA/RG composites is made with respect to their structure, mechanical, electrical, and some thermal properties as the most representative characteristics essential for most materials. In addition to the systematic evaluation of these assembly techniques and material engineering concepts, our study also leads to materials with record high toughness among other layered composites and better understanding of the supporting structural reasons. This study also demonstrates that electrical properties in these composites are primarily determined by atomic and nanoscale structural parameters that are markedly different in these composites. Mechanical properties are, nevertheless, nearly identical especially for high RG content LBL and VAF composites, except the case of covalent cross-linking. All aspects of mechanical performance can be rationalized considering the thermodynamic state of the polymer at the RG interface.

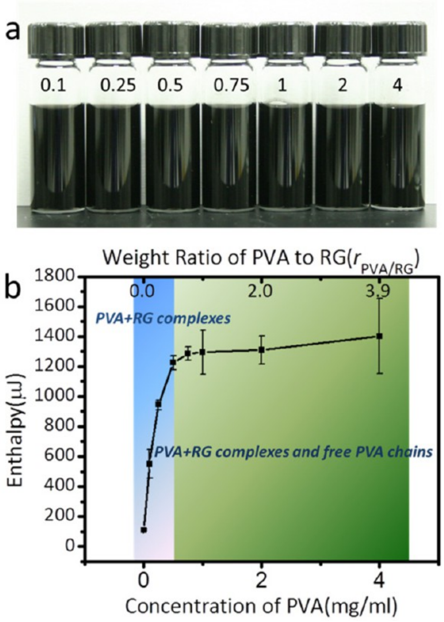

Figure 1. (a) Photograph of dispersions from PVA and RG at different weight ratios. (b) Mixing enthalpies of PVA and RG for different PVA/RG ratios.

RESULTS AND DISCUSSION

PVA and RG Interactions. RG and PVA were chosen as the basic components for LBL *vs* VAF evaluation for the following reasons:

(1) Both VAF and LBL composites can be made from RG and PVA. Moreover, the fractions of polymer and nanoscale component in the RG/PVA system could be nearly identical for both methods,[1,10,18,21] allowing adequate comparison of the two techniques.

(2) Each component of the RG/PVA composites has important contributions to the properties of the resulting material. RG is well known for its mechanical,[22] electrical,[23] and thermal[24] characteristics. A combination of all these factors makes the comparison comprehensive. It also opens up the possibility of finding the structure−property relationships for hard-to-reach multiparameter combinations. Note also that RG is a better alternative than graphene oxide (GO), clays, or other wide-band-gap nanomaterials despite passing the criterion (1) because of the multiple functional properties available for comparison.

(3) Systematic evaluation of LBL *vs* VAF materials assembly methods also enables us to improve performance characteristics of RG composites, reducing, for instance, brittleness and increasing toughness. This study provides an opportunity to evaluate VAF and LBL as tools for this common problem.[11]

The atomic and nanoscale engineering of the interface in layered nanocomposite assemblies relies on specific interactions between polymers and inorganic components. Noteworthy is the fact that such interaction could be problematic for VAF, as it could lead to coagulation prior to the successful assembly process.

On the other hand, strong specific interactions of macromolecules represent the foundation of the LBL assembly. They are also essential for high mechanical performance. Adequate VAF *vs* LBL comparison requires these interactions to be strong enough to afford LBL but not too strong to cause premature coagulation of components in the VAF technique.

A series of PVA and RG mixtures display no agglomeration in a wide range of PVA/RG weight ratios, $r_{PVA/RG}$ (Figure 1a). At the same time, isothermal titration calorimetry (ITC) analysis indicates an exothermic process in the mixing of PVA and RG (Figure S1a). This observation indicates attractive interactions between the components. The mixing enthalpy initially increases linearly and then reaches a plateau for $r_{PVA/RG} > 0.55$ (Figure 1b). The total enthalpy is measured by integrating heat rate and time curve after reaching a thermal equilibrium state (Figure S1a). Note that dilution enthalpy of PVA plays a very minor role in the total mixing enthalpy, as it varies little with PVA concentration (Figure S1b). Such behavior suggests that specific interactions between PVA and RG attain their maximum at $r_{PVA/RG} = 0.55$, which will be reflected in mechanical and other properties of PVA/RG composites.

The primary contributors to the interactions between RG and PVA are believed to be hydrogen bonds between abundant $-$OH groups on PVA chains and $-$OH/$-$COOH groups on RG sheets. van der Waals forces, hydrophobic attractions, and charge transfer between polar functionalities in PVA and π-conjugated domains[4] in RG can also bind PVA to RG. Mixing enthalpy increases with PVA concentration until all possible adsorption sites on the RG surface are occupied, which explains the plateau for $r_{PVA/RG} > 0.55$. Beyond this threshold, further addition of PVA increases the concentration of "free" polymeric chains in solution.

Preparation of LBL and VAF Composites. LBL assembly was realized using the classical approach by alternatively dipping a glass substrate in PVA solutions and RG dispersion with intermittent rinsing with water (Figure 2a). The assembly process was monitored by the absorbance change at 550 nm (Figure 2b) and quartz crystal microbalance (QCM, Figure 2c). Both techniques indicate that the RG+PVA LBL system has a linear and uniform multilayer growth with an increment of 1$-$2 nm in thickness or 0.2$-$0.4 μg/cm^2 of mass per layer (Figure 2c). As indicated by QCM, the concentrations of PVA, RG, and corresponding immersion time affect the growth pattern of the multilayers, which allows us to control RG fractions in the resulting LBL

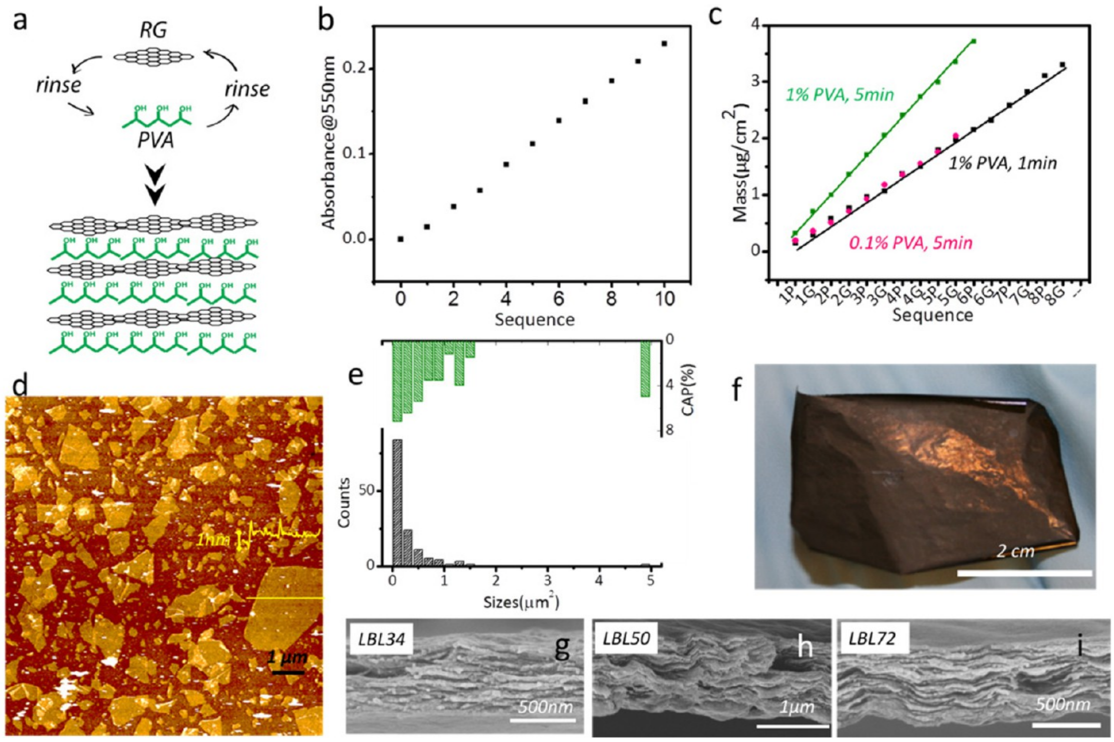

Figure 2. Layer-by-layer (LBL)-assembled PVA/RG composites. (a) A schematic drawing of LBL assembly. (b) UV$-$vis absorbance of a PVA/RG LBL film grown on a glass substrate at 550 nm for different numbers of deposition cycles. (c) QCM weight per area data for different numbers of deposition cycles and LBL deposition conditions. (d) AFM image of one bilayer of PVA and RG deposited on a silicon substrate. (e) Number and cumulative area percentage (CAP) of RG nanosheets of different sizes calculated from AFM images. (f) Photograph of a piece of freestanding LBL50 film. (g$-$i) Scanning electron microscopy images for the cross-sectional areas of LBL34, LBL50, and LBL72.

composites. In this study a series of 300-bilayer films with different $r_{PVA/RG}$ are prepared. These composite samples contained 34 wt %, 50 wt %, and 72 wt % of RG; they are denoted as LBL34, LBL50, and LBL72, respectively.

An approximately 1 nm thick film of RG sheets adsorbs on a smooth and uniform layer of PVA with a dominantly flat orientation in each dipping cycle (Figure 2d). RG sheets with an area of $<0.2\ \mu m^2$, $0.2-0.6\ \mu m^2$, and $>0.6\ \mu m^2$ cover 7%, 12%, and 19% of the total area of the substrate surface (Figure 2e), respectively. More than 50% of the nanosheets are smaller than $0.2\ \mu m^2$ (Figure 2e). Although a belief that bigger sheets can give rise to better mechanical performance exists,[3] current studies on graphene do not support this idea.[25]

The layered structures for LBL composites (Figure 2e) can be seen in the cross-sectional SEM image (Figure 2g−i). The total thickness of LBL50 after 300 dipping cycles is 1000 ± 10 nm (Figure 2h), which is almost 2 times greater than that of LBL34 (575 ± 25 nm) and LBL72 (500 ± 7 nm) obtained after the same number of cycles (Figure 2g and i). In the preparation of LBL50, longer immersion time in each LBL cycle stimulates the adsorption of both species, producing a state with a nearly thermodynamically optimal ratio between RG and PVA (see Figure 1). It corresponds to the completion of adsorption sites on RG available for PVA while no minimal free PVA is present. In the case of LBL34 the coverage of RG is incomplete, while for LBL72 some of the free polymer remains, therefore shifting all the properties toward those of free polymer. The balanced adsorption of PVA and RG also leads to thicker films, which also accelerates the deposition. The time needed to make 1 μm thick LBL50 including solution preparation and delamination from the substrate is *ca.* 115 h, in comparison to the *ca.* 195 h for 1 μm thick LBL34 and LBL72.

VAF assembly was carried out by mixing 10 mg/mL PVA and 0.14 mg/mL RG aqueous solutions together at different volume ratios. PVA and RG slowly assemble on top of each other as the film settled down on a nylon filter under vacuum and transitions from a semi-ordered gel to the layered structure (Figure 3a).[26,27] Typically, it takes 48 h to assemble a piece of 20 μm film. The overall rate of assembly is 2.4 h/μm, much faster in comparison to 115 h/μm for the LBL process.

The fraction of RG can be adjusted by altering $r_{PVA/RG}$ (Figure 1a). The RG content in VAF composites was determined by TGA (Figure S2) to be 85%, 60%, 50%, 46%, and 27%; the corresponding samples were labeled as VAF85, VAF60, VAF50, VAF46, and VAF27, correspondingly. Note that if $r_{PVA/RG} > 0.55$, PVA is present in the dispersion with RG as free chains and as a complex with the nanosheets. Most of the free PVA is retained in the material during the vacuum filtration process; otherwise we would not be able to have an RG content below 45%. The presence of these free chains and their mode of packing among the RG sheets makes, as we shall see below, a significant effect on the properties.

The stability of both LBL- and VAF-assembled films was tested in boiling water for 20 min, under which

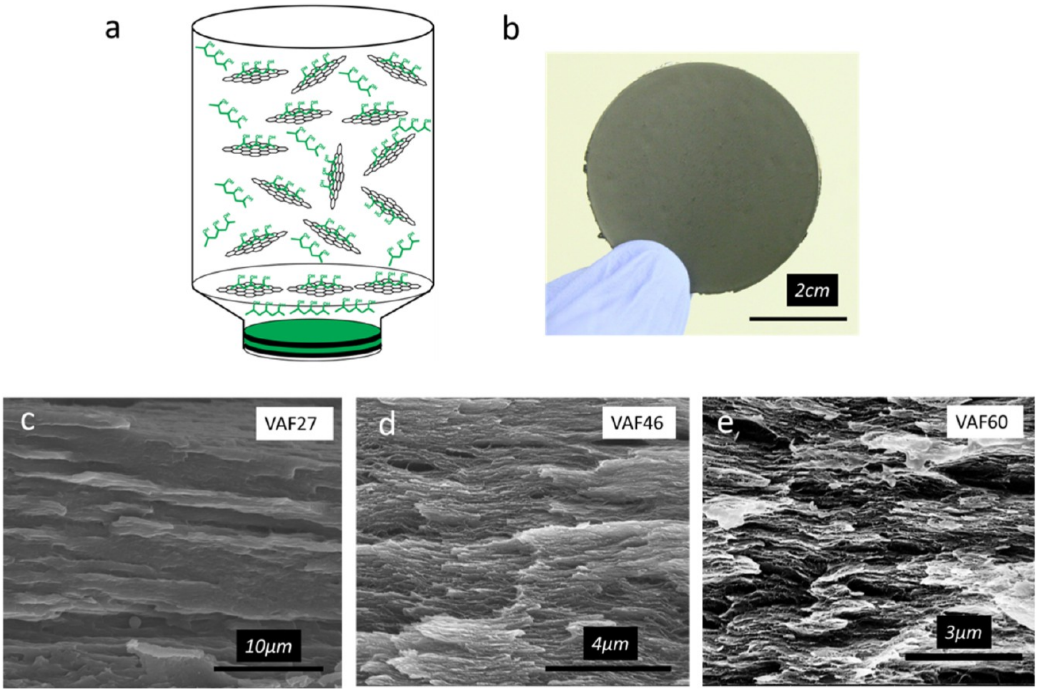

Figure 3. Vacuum-assisted flocculation (VAF) of PVA/RG composites. (a) A schematic drawing of VAF assembly. (b) Photograph of a piece of freestanding VAF60 film. (c, d, e) Scanning electron microscopy images for the cross-sectional areas of VAF27, VAF46, and VAF60.

pure PVA was easily dissolved. Both types of films show no sign of material loss except for VAF27, whose thickness decreased from 56 μm to 40 μm. The excessive free PVA chains can easily escape from the confined nanochannels in VAF27. For other VAF films, however, strong interactions between PVA and RG plus the geometrical confinement prevent the loss of polymers. Films made by LBL assembly, however, can survive the intense conditions even for LBL34 due to the rinsing/drying steps for removing the loosely bonded polymers.

Structural Comparison. Both LBL and VAF assembly produce materials with well-defined layered structures (Figures 2 and 3). The alignment of RG sheets appears to be more pronounced for the LBL than VAF composites. The anisotropy of LBL- and VAF-made stacks of nanosheets can be quantified by X-ray diffraction (XRD) patterns especially when the X-ray beam is directed from their side/edge (Figure 4a and b). The films appear to be mostly isotropic when the X-ray beam is directed normal to the surface of the films (Figure 4c and d). Two characteristic repeating distances of ~0.4 nm ($2\theta \approx 20°$) and ~1.75 nm ($2\theta \approx 5°$) are evident in the XRD profiles for both LBL and VAF materials (Figure 4e,f,g,h). Previously published XRD studies of similar composites[10,14,18] indicate that the Bragg diffraction peaks and shoulders at $2\theta \approx 5°$ should be attributed to the diffraction from adjacent RG sheets. The repetitive distance between sheets in layered materials is also known as basal spacing. The peaks at $2\theta \approx 20°$ correspond to the diffraction from the $[10\bar{1}]$ plane of PVA crystallites, which was previously observed in neat PVA (Figure 4e).[28,29]

In VAF composites, the consistent shift of the ~5° shoulder/peak toward lower 2θ values with increasing PVA content (Figure 4e) indicates enhanced intercalation of the polymer between RG sheets, which confirms the assignment of the peak as its disappearance in the X-ray diffractograms obtained with perpendicular orientation of the beam (Figure 4g). VAF46 displays a spacing of 1.9 nm, as compared to 0.36 nm for the RG paper that does not contain PVA at all (Figure S3a). VAF27 shows no such peak, possibly due to shift of the peak beyond the lower 2θ limit of the XRD instrument or complete lack of regularity (Figure 3).

It is worthwhile to make a brief sideline comparison to VAF-assembled composites from GO. The interlayer spacing of the PVA/RG composites is larger at a similar weight fraction of the nanosheets than in PVA/GO composites (Figure S3b). This observation suggests that the larger number of functional groups of GO leads to stronger intermolecular interactions and more proximate positioning of PVA chains to the sheets of GO than to RG.

Continuing with VAF composites, PVA $[10\bar{1}]$ XRD peaks at $2\theta \approx 20°$ change with RG content. However, this change is different for PVA crystallites aligned along the RG surfaces and those formed beside the RG, which are presumably from free PVA chains present in solution (Figure 4j). They can be denoted as peripheral crystallites. The anisotropy of the PVA crystallites is obvious in the XRD diffraction patterns (Figure 4a) when the X-ray is directed through the side of the film. This behavior indicates the epitaxial effect of the RG surface with respect to the growth of PVA crystallites,[30] which are aligned along the RG sheets (Figure 4j). A similar behavior was observed for TiO_2 crystallites confined between the adjacent polymer layers.[31] These crystallites lead to the anisotropic patterns (Figure 4a) diffracting from $[10\bar{1}]$ planes parallel to the RG surface. For composites with higher RG content, the $[10\bar{1}]$ peak shifts to a higher 2θ region, indicating decreased spacing from 0.45 nm to 0.43 nm (Figure 4e). It was once observed that the introduction of clay nanosheets can promote new phase formation of PVA.[28] The precise control over organic crystallites' spacing was only reported recently through lattice straining effect via shearing,[32] while in our case the mechanism to introduce lattice strains is clearly different. It is likely that the capillary effect of different sized RG nanochannels causes varied compressive stress and thus strain on the PVA crystallites during their formation with the removal of water. The smaller the basal spacing, the stronger the effect is. In comparison, randomly distributed peripheral PVA crystallites (Figure 4j) demonstrate isotropic diffraction rings in the XRD images when the X-ray beam is perpendicular to the surface (Figure 4c). The $[10\bar{1}]$ peak in the random PVA crystallites shows no dependence on the RG content (Figure 4f). Interestingly, in the PVA/GO composites, PVA crystallites are absent according to XRD spectra obtained under similar conditions and only reappear after the reduction of GO.[14,18] This fact suggests that the strong interaction with GO prevents PVA crystallization. In contrast, RG sheets with milder interactions with the polymer allow for additional degrees of freedom for the PVA chains on the surface of RG and, therefore, facilitate their crystallization.

The XRD profiles of LBL-assembled composites also display a shoulder peak at ~5° (Figure 4f). The signal for RG basal spacing is less defined for LBL than for VAF assemblies because LBL films are thinner; however it is clearly located at $2\theta > 5°$, while the same peak corresponding to the basal spacing of VAF composites is located at $2\theta < 5°$ at any RG content (Figure 4e,f). A clear case comparison is LBL50 ($2\theta = 5.0°$ shoulder) *vs* VAF46 ($2\theta = 3.6°$ shoulder) and VAF60 ($2\theta = 4.0°$ peak). We conclude that for the same RG content the basal spacing in LBL composites is generally smaller than for VAF composites. Similarly

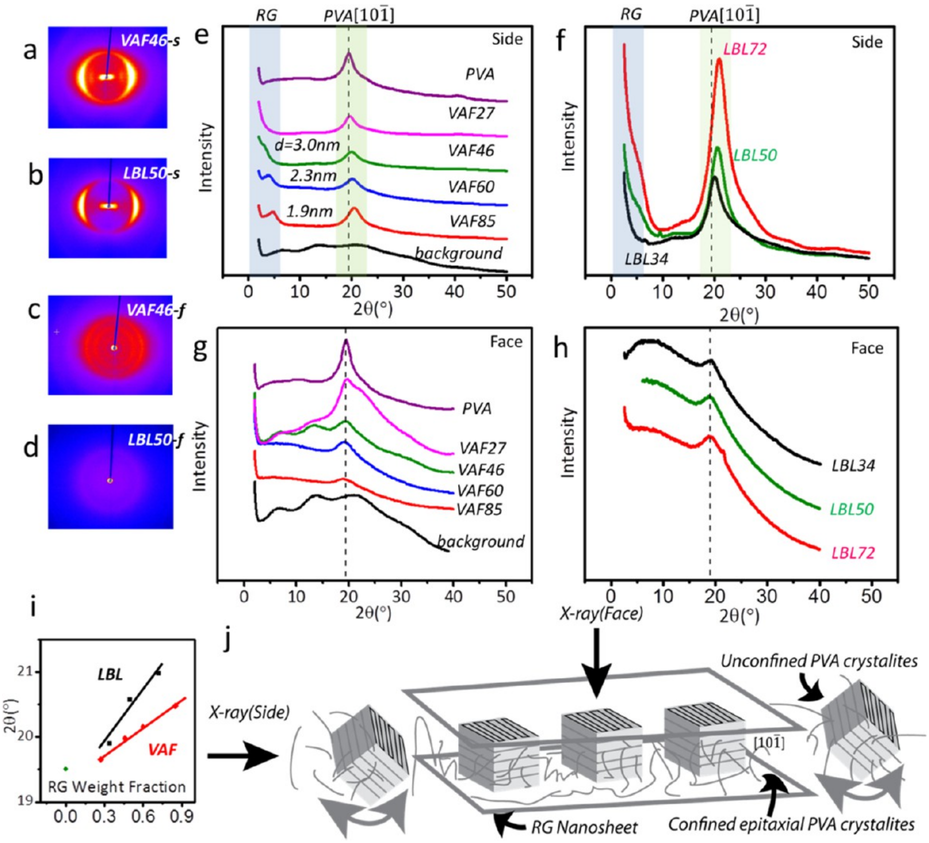

Figure 4. X-ray diffraction spectra for PVA/RG composites. (a, b, c, d) XRD images for VAF (a, c) and LBL (b, d) composites with the X-ray beam directed at the side (a, b) and through the face (c, d) of the samples. (e, f, g, h) XRD profiles for VAF (e, f) and LBL (f, h) composites with the X-ray beam directed at the side (e, f) and through the face (g, h) of the samples. The intensity of the XRS profile is shown in the linear scale. (i) Dependence of the X-ray scattering angle for PVA crystallites on the RG content for VAF and LBL composites. (j) A schematic of confined epitaxial and peripheral PVA crystallites.

to VAF-made materials, the signal from RG basal spacing shifts toward larger 2θ values with increasing RG content (Figure 4f).

The LBL composites also reveal the presence of "epitaxial" and peripheral PVA crystallites similarly to the VAF composites. The anisotropy of PVA crystallites for the PVA $[10\bar{1}]$ peak at $2\theta \approx 20°$ in LBL-made materials is visibly greater (Figure 4b *vs* d and Figure 4f *vs* h), which is indicative of the lower contribution of the peripheral than from epitaxial PVA crystallites. The position of the corresponding XRD peak shifts with different RG contents and shows similar differences of face- and side-directions of the X-ray beams as in VAF composites, although greater. As the content of RG increases, the PVA $[10\bar{1}]$ plane spacing decreases from 0.454 nm ($2\theta = 21.0°$) in pure PVA to 0.423 nm ($2\theta = 19.5°$) (Figure 4f).

PVA crystallites in LBL- and VAF-assembled composites (Figure 4i) display distinct structural differences as well. At similar RG content, the LBL-assembled composites tend to have higher 2θ or smaller PVA $[10\bar{1}]$ plane spacing than VAF composites. This fact suggests that in LBL composites PVA interacts with a larger area of RG than in VAF composites. In other words, the LBL process is more effective in epitaxial templating of PVA crystallites due to greater degrees of freedom available to the PVA chains at the substrate–solution interface when it has to adapt its conformation to the substrate.[33]

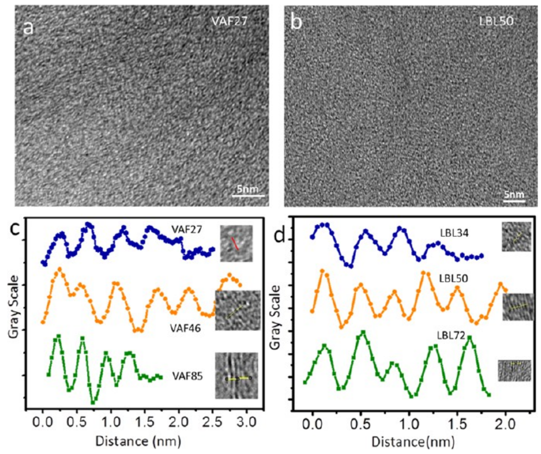

Figure 5. High-resolution TEM images of (a) VAF27 and (b) LBL50 cross sections. Variation of the gray scale along the scan for (c) VAF- and (d) LBL-made composites.

The nanoscale stacking patterns in the VAF and LBL composites were further confirmed by high-resolution transmission electron microscopy (HR-TEM) and selected area electron diffraction (SAED, Figures 5 and S4). All VAF- and LBL-made films show a similar length scale of 0.4 nm for the layer spacing, with VAF27 and LBL34 slightly larger in their own categories. This observation complies with the basal spacing of PVA crystallites in the XRD results (Figure 4). It is difficult, however, to observe the longer range periodicity corrresponding to the arrragement of RG, which is possibly due to the poor imaging contrast between RG and PVA crystallites. Overall, LBL films shows more uniform layer distribution in comparison with VAF ones (Figures 5 and S4).

Thermal Properties. A great advantage of combining nanoscale components and polymers is enhanced thermal stability associated with profound changes in chain dynamics and reduced gas permeability to avoid oxidation.[13,34] According to differential scanning calorimetry (DSC), both LBL and VAF composites show marked suppression of glass transition of the matrix material (Figure 6a,b). Glass transition temperature can be identified as a DSC "step" corresponding to a second-order endothermic phase transition, while melting shows up as a first-order phase transition appearing as a peak.[35] Neat PVA (Figure 6a, black trace) demonstrates a glass transition temperature (T_g) of 75 °C and pronounced melting temperature (T_m) of 218 °C in the heating curve (Figure 6a)[28] followed by crystallization upon cooling at 165 °C.

The T_g of VAF27 is increased by 10 °C, while T_m is reduced by 20 °C compared to pure PVA (Figure 6a *vs* b). Concurrently, LBL34 displays an increased T_g by 25 °C without defined T_m (Figure 6c). The changes in T_g and T_m are more pronounced for LBL- than for VAF-assembled materials. This finding supports the conclusion that polymer chains are constrained between RG sheets in LBL composites more strongly than in VAF composites.[36] The further increase of RG fraction leads to the complete suppression of the glass transition point in both LBL- and VAF-assembled films (Figure 6b and c). Such thermal behavior is quite similar to many "neatly intercalated" clay composites.[28] Note also that the effect of clay on the T_m is different in other layered materials, such as PVA/clay composites. It was reported that the composites exhibited a dual melting point as compared to a single melting point of neat PVA due to phase separation of syndiotactic and atactic PVA.[28]

Mechanical Properties. We then systematically investigated and compared the mechanical properties of LBL- and VAF-made PVA/RG composites, namely, their Young's modulus (E), storage modulus (E'), ultimate strength (σ_{ult}), ultimate strain (ε_{ult}), and toughness (K). PVA/RG composites made by both methods display progressively higher E and E' with increasing RG content (Figure 7a) and demonstrate overall high mechanical performance (Table 1). The properties of LBL and VAF differ greatly when the RG volume fraction is low, while becoming more similar for high RG contents. Neat PVA shows $E = 3.5 \pm 0.2$ GPa and $\sigma_{ult} = 90 \pm 5$ MPa. With addition of 27 wt % RG, the VAF27 shows, slightly higher, $E = 4 \pm 0.3$ GPa and $\sigma_{ult} = 95 \pm 7$ MPa. In contrast, the addition of 34 wt % RG via LBL improves both properties of the film by almost 2 times to $E = 7 \pm 0.5$ GPa and $\sigma_{ult} = 160 \pm 11$ MPa. This result is attributed to the better plane-oriented RG sheets via the bottom-up alternative stacking of PVA and RG in LBL (Figure 4). At higher RG content, the mechanical performance difference shown in LBL72, LBL50, VAF85, VAF60, and VAF50 is minor (Figure 7a and b). The differences at atomic and nanometer scales observed in XRD between these composites are apparently less influential for these materials; the reasons behind this similarity and apparent inconsequentiality of atomic and nanoscale features are discussed below. It is not entirely unexpected that the existing theoretical models such as Voigt,[37] Reuss,[37] Padawer and Beecher,[37,38] Riley,[37,38] Mori—Tanaka,[39] and Halpin—Tsai[40] equations give poor predictions of the Young's modulus of our composites (Figures 7c and S6g), either overestimating (Voigt, Padawer and Beecher, Riley, Mori—Tanaka, and Halpin—Tsai) or underestimating (Reuss) the experimental values. The reasons for failure of these models to predict correctly the mechanical properties are multiple. The most essential problem of these models appears to be in the assumption of the ideal stress transfer at the RG—polymer interface. Uncertainty about the atomic, molecular, nanometer, and submicrometer scale mechanics at these interfaces

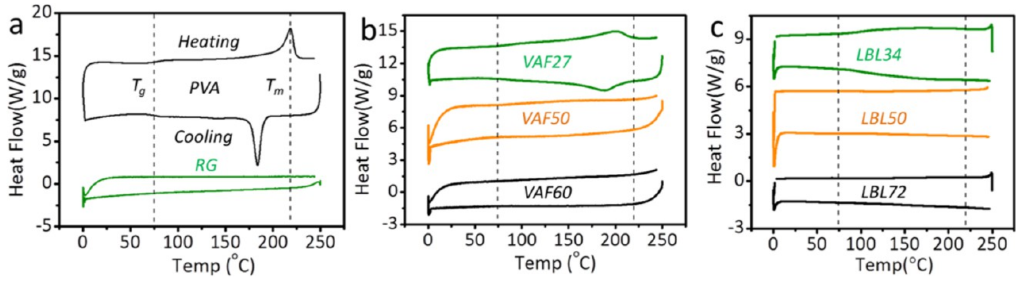

Figure 6. DSC curves for (a) neat PVA and RG VAF assembly without a polymer, (b) VAF composites, and (c) LBL composites. Zoomed-in curve for VAF27 demonstrating that the glass transition point of the composite can be found in Figure S5.

does not allow researchers to develop better models. It is also unclear whether the Reuss model with the "serial" coupling of matrix and the filer would be applicable to layered composites with parallel orientation of both soft and hard components.

The RG–PVA interaction and the interface between them are *de facto* described empirically from the perspective of thermodynamics in Figure 1. Therefore, one can raise the question whether there would be some correlation between the mechanics and thermodynamics of the composites. In this respect one can see that the point of inflection of the curve in Figure 1b describing the enthalpy of the RG–PVA system occurs for a volume fraction of 53.5%. The inflection point on the tensile strength curve occurs at *ca.* 40% for both VAF and LBL composites in Figure 6d. At the same time, we do not see any particular inflections on the dependence of Young's modulus *vs* volume fraction in Figure 6c.

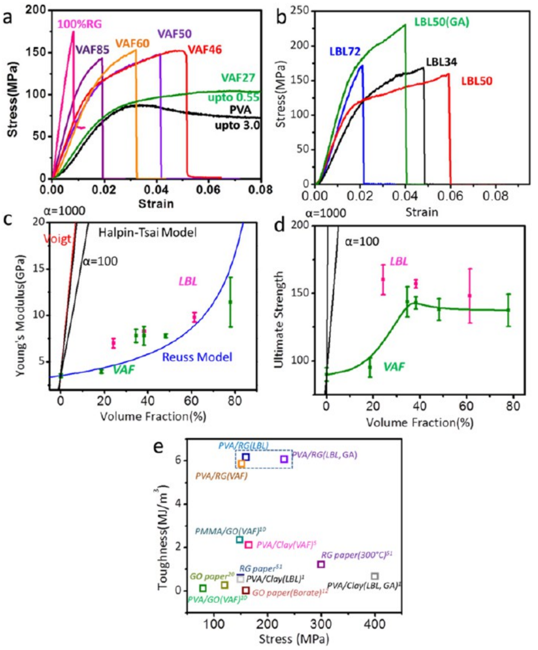

Figure 7. Mechanical properties of PVA/RG composites. (a, b) Stress–strain curves for VAF (a) and LBL (b) composites. The full range for VAF27 and PVA is shown in Figure S6b. (c) Young's modulus prediction based on the Voigt (red), Reuss (blue), and Halpin–Tsai (black) equations for different aspect ratios of the filler (α). (d) Comparison of calculated and experimental data for ultimate strength of RG composites. (e) Comparison of PVA/RG composites with other GO, RG, and clay composites in the toughness–strength chart.

Thermodynamics of RG–PVA interactions should have a strong influence on the energy expenditures required for composite deformation. Therefore, it would be meaningful to look at the toughness of the prepared composites. As one can see in Figure 7, the volume fraction of *ca.* 50% RG corresponding to the case when all the polymer chains are interacting with the RG surface also leads to increased *K*. Moreover, we observed that in both VAF and LBL cases this composition gives the unique combination of ultimate tensile strength and toughness with $\sigma_{\mathrm{ult}} \approx 150$ MPa and $K \approx 6.1$ MJ/m^3. One could also point out that this RG content of 50% is close to the brittle to ductile transition point, which makes sense since the excess of easily deformed PVA will compromise mechanical strength. So, the hypothesis about the correlation between the thermodynamics of polymer–filler interactions and its mechanical performance appears to us plausible. At the same time, its thorough evaluation will need a more extensive investigation than a single paper.

Continuing with mechanical properties, we cannot help but notice that this combination of σ_{ult} and *K* is best among various layered GO, clay, or RG composites previously studied (Figure 7c). In general, strength and toughness are two mutually exclusive properties, which usually require a reduction of one to improve the other.[41,42]

Glutaldehyde (GA), capable of aldehyde–hydroxyl cross-linking, was reported to increase the strength and/or toughness of the layered composites. The samples of LBL50 and VAF46 were treated by 10 wt % GA overnight to understand the effect of potential cross-linking on the mechanical properties of PVA/RG composites. The GA treatment increases *E* to 13 GPa and σ_{ult} to 222 MPa for LBL50 (Figure 7b, Table 1), while it has no effect on VAF-assembled composites. This fact

TABLE 1. Mechanical Properties of PVA/RG Composites Made by LBL and VAF Assemblies

		storage modulus (GPa)	stiffness (GPa)	strain	tensile strength (MPa)
	RG	19.02 ± 1.34	19.87 ± 2.55	0.01 ± 0.002	193 ± 30
	PVA	3.01 ± 0.25	3.52 ± 0.18	2.5 ± 0.5	90 ± 5
VAF	VAF85	13.1 ± 1.26	11.41 ± 2.68	0.022 ± 0.003	137.5 ± 4.5
	VAF60	9.13 ± 1.13	7.8 ± 0.2	0.031 ± 0.001	138 ± 12
	VAF50	8.42 ± 0.58	7.8 ± 1	0.051 ± 0.013	143.1 ± 11.2
	VAF46	9.51 ± 2.47	7.8 ± 0.7	0.046 ± 0.006	143.7 ± 8.1
	VAF27	4.00 ± 0.34	3.97 ± 0.20	0.48 ± 0.08	95 ± 7
LBL	LBL72	10.2 ± 0.75	9.8 ± 0.5	0.017 ± 0.002	148 ± 20
	LBL50	8.1 ± 0.28	8.3 ± 0.1	0.056 ± 0.004	157 ± 3
	LBL34	7.6 ± 0.83	7 ± 0.5	0.044 ± 0.013	160 ± 11
	LBL50(GA)	13 ± 0.52	13 ± 2	0.041 ± 0.005	222 ± 18

can be attributed to the difference in nanoscale structure between the two different types of composites. Both VAF and LBL films have excellent barrier properties; thus the amount of GA that penetrates into the bulk of the films is small. In the case of LBL the polymer exists primarily at the interface with RG, where the cross-linking occurs. In the case of VAF composites, PVA chains have a smaller area of contact with the RG sheets. We believe that GA preferentially cross-links PVA molecules themselves rather than creating covalent bonds between the polymer and RG. Since PVA is already stiffened due to constrained volume (see Figure 6), the net effect on mechanical properties is negligible. Despite the dramatic decrease or increase of toughness reported for PVA/clay[1] or PVA/CNT[2] composites, GA cross-linking does not affect the toughness of LBL50 material (Figure 7c).

Comparison of the structural data and mechanical and thermal properties warrants additional discussion. A layered architecture typical of aligned RG sheets established by SEM imaging is associated with micrometer and submicrometer levels of organization. At this structural level VAF and LBL composites display clear similarities. On the other hand, their atomic and nanometer scale features revealed in AFM, XRD, and TGA data are different. In this respect, the findings about *mechanical properties of VAF and LBL composites are surprising because the differences in atomic and nanoscale structure have unexpectedly little influence on the mechanical properties of VAF and LBL composites especially with high RG contents* (compare LBL50 and LBL72 *vs* VAF46, VAF50, VAF60, and VAF85) (Figure 7a and b, Table 1). One might conclude that the similarities of mechanical properties at high RG content are associated with similarities at the micrometer and submicrometer scale. However, this conclusion is not valid. The evidence that atomic scale and nanoscale structures are still influential for the layered composites can be found in the results obtained after the GA treatment that improves Young's modulus and tensile strength for LBL composites but does not change the mechanical properties of VAF composites due to covalent cross-linking at the RG−PVA interface.

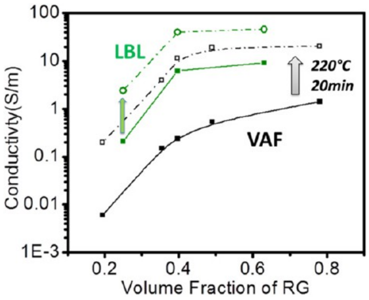

Figure 8. In-plane electrical properties of LBL (green) and VAF (black) composites before (solid lines) and after (dashed lines) incubation at 220 °C for different RG fractions. The experimental errors are displayed but are too small to be shown in the graph.

Considering (a) the inability of the existing models (Figure 7c,d) to describe the mechanics of the composites adequately and (b) our expectations how strongly the atomic/nanoscale morphology should affect the mechanical performance, the hypothesis about the correlation between thermodynamics of the RG−PVA interaction and mechanics of the resulting composites can help us explain the experimental observations. Conceptually, the mechanical properties of the composites could be rationalized from the standpoint of the thermodynamic state of the polymer at the RG−PVA interface. Reaching a thermodynamic minimum of PVA chains on the surface of nanosheets leads to stronger, stiffer, and tougher materials than those formed with suboptimal packing polymer at this boundary. In other words, minimization of the energy of the macromolecule in contact with the RG surface improves stress transfer and energy dissipation. As a consequence, we see the highest toughness for LBL50 and VAF46 composites (Figure 4c) among all other filler contents. The weight composition for the high toughness material is identical to that of the RG−PVA complex observed in solution (Figure 1). The role of the adsorption state thermodynamics can also be traced in the similarities and differences of mechanical properties of LBL and VAF composites. In the case of VAF composites with high RG content, the relative amount of epitaxial *vs* peripheral PVA crystallites is different, and the alignment of nanosheets is less regular than in LBL (Figure 4), but most of the PVA at the RG interface is in the optimal conformation, corresponding to the thermodynamic minimum, which is the same for LBL and VAF materials. Thus the mechanical properties are similar as well.

At the moment we cannot identify the reasons that the dependence of Young's modulus on RG content in Figure 7c does not appear to have an inflection point for an RG content of ∼50%. Part of the reason may be different mechanisms of elastic deformations for small strains compared to large strains responsible for ultimate tensile strength and toughness.

Electrical Properties. The in-plane conductivity of the as-made PVA/RG LBL composites is more than 1 order of magnitude higher than that of VAF-made composites at similar RG content (Figure 8). Thermal treatment and related chemical changes in RG improve the conductivity while reducing the difference in charge transport performance between the two types of materials. After incubation at 220 °C, causing further restoration of the graphitic network of sp^2-hybridized carbons in RG,[43] the conductivity reaches 46 and 12 S/m for LBL and VAF composites, respectively. These electrical properties are better than most reported RG composites.[44]

The large disparity in electrical conductivity is a clear representation of their structural differences at the atomic and nanoscale levels of organization. The greater contents of randomly oriented peripheral PVA crystallites and larger basal spacings observed for VAF composites in XRD studies (Figure 4) lead to the conclusion that the average separation between the conductive RG sheets in LBL composites is smaller than in VAF composites. With respect to micrometer and submicrometer scales, the improved alignment of RG sheets in the LBL assembly as compared to their organization in VAF composites (Figure 4) enhances their overlap. It is common to observe several pieces of RG overlapping each other in the AFM image of LBL bilayers (Figure 2d). In contrast, most individual RG sheets in the VAF assembly are surrounded by PVA, which serve as an insulating interface.

CONCLUSIONS

LBL and VAF are widely used methods for making advanced composites. From previous work we could infer that LBL assembly can be favored in terms of better control of nanoscale organization and applications toward microscale devices,[45−48] while VAF composites as well as exponential LBL[49] can be more advantageous for applications where a large volume of the material is needed. The novelty of the study carried out here is that comparison of LBL- and VAF-made materials creates a conceptual framework for property-oriented materials engineering of layered composites. Multiple structural factors at different RG contents were correlated with thermal, electrical, and mechanical properties. Molecular processes, such as epitaxial crystallization of PVA on RG, that were not identified before in RG−polymer systems were clearly demonstrated. They are essential for the understanding of composite properties. The structural effects on electrical conductivity were consistent with *a priori* expectations favoring LBL assembly that minimizes tunneling barriers between conducting sheets. The unexpected lack of correlation between nano- and microscale structural features and mechanical properties was also observed. The findings about mechanical properties were rationalized based on enthalpic effects at the organic−inorganic interface. We believe that reaching the energy minimum for polymer chains adsorbed to nanosheets plays a critical role in the improvement of mechanical properties, while the other structural parameters are secondary. Notably we made LBL and VAF composites with a toughness of 6.1 MJ/m^3, which is the highest among any layered composites from RG, cellulose, clay, and similar materials. Optimization of the mechanical properties from the perspective of thermodynamics rather than the purely morphological perspective appears to be a universal and quantifiable approach that could be extended to a variety of other composites. Application of the thermodynamic approach to the design of organic−inorganic materials may simplify the process of materials engineering.

METHODS

Preparation of Graphene Oxide. GO can be made by a modified Hummers method from graphite powders (Bay carbon, SP-1).[50] In a typical reaction, 1 g of graphite, 1g of $NaNO_3$, and 50 mL of H_2SO_4 were stirred together in an ice bath, and 6 g of $KMnO_4$ was then slowly added. The solution was then transferred to a 35 °C water bath and stirred for about 1 h. Then 80 mL of water was subsequently added, and the solution was stirred for 30 min at a temperature of 90 °C. Finally, 200 mL of water was used to dilute the mixtures, followed by addition of 6 mL of H_2O_2 (30%). The warm solution was then filtered. The GO slurry collected from membrane was then washed with 300 mL of 2 M HCl, and purified GO can be collected at the tube bottom after centrifugation. The GO was further purified by dialysis for one week, and GO powder was made by lyophilization. Typical Raman spectra are shown in Figure S7. The elemental analysis shows that the mass ratio of C:O:N is 43:54:3 in GO.

Preparation of Chemically Reduced Graphene Dispersions. The RG dispersion was made according to a report by Li *et al.*[51] A 62.5 mg sample of GO was dispersed by tip-sonication in 100 mL of DI water for 20 min. An additional 150 mL of DI water, 75 μL of 50 wt % hydrazine, and 875 μL of ammonia solution were then added. The mixture was then heated to 90 °C for 3 h, and a homogeneous graphene dispersion was obtained. The concentration of the RG solution was calibrated by weighing the RG paper formed by filtration and was around 0.14 mg/mL. The elemental analysis shows that the mass ratio of C:O:N:H is 82:13.5:3.5:1 in RG. The comparison of GO and RG Raman spectra is shown in Figure S7.

Layer-by-Layer Assembly of Polyvinyl Alcohol and RG. In a typical LBL cycle, glass slides cleaned by piranha solution for 24 h were immersed in 1 or 0.2 wt % PVA (Aldrich, Mowiol 56−98, M_w ~195 000) for 2−5 min, rinsed with DI water, and then dried with compressed air. Subsequently, these slides were dipped into the 0.05−0.14 mg/mL RG dispersions for 2−5 min, followed by rinsing and drying. A total of 300 bilayer films were deposited on a glass substrate by a NanoStrata robot. Modified deposition conditions for preparations of LBL composites with different RG content could be described as [PVA(*a*)-*m*/RG(*b*)-*n*], where *a* and *b* are the concentration of PVA and RG in mg/mL; *m* and *n* are the dipping time in units of min for each solution. The RG fractions for films under conditions of [PVA(10)-15/RG(0.05)-2], [PVA(10)-5/RG(0.14)-5], and [PVA(1)-2/RG(0.14)-5] were 34 wt %, 50 wt %, and 72 wt %, and the corresponding films were labeled LBL34, LBL50, and LBL72 for simple discussions. The volume fractions of the composites were calculated with the PVA density of 1.3 g/cm^3 and RG density of 2.1 g/cm^3.

Vacuum-Assisted Flocculation of PVA and RG. A 100 mL amount of 0.14 mg/mL RG dispersion was mixed with 2, 3, 4, and 6 mL of 10 mg/mL PVA, briefly sonicated, and then filtrated through a 0.1 μm pore size nylon membrane under vacuum over the course of 2 days. The film was peeled off from the filter and dried in the vacuum oven. The films were labeled VAF85, VAF60, VAF50, VAF46, and VAF27 according to RG fractions in the films.

Characterization. The LBL process was monitored by an 8453 UV−vis ChemStation spectrophotometer from Agilent Technologies. The growth of the film was also investigated by a quartz crystal microbalance 200 from Stanford Research Systems. Quartz crystals of 5 MHz were used in all the studies. Cross-sections of the films were examined by FEI NOVA Nanolab scanning electron microscopy (SEM). Transmission electron microscopy (TEM) images were collected by a JEOL 3011

HRTEM. Samples were sliced ~70 nm thick by an ultramicrotome, followed by deposition on a copper grid.

Differential scanning calorimetry was carried out on a TA Instruments Q2000 DSC under a nitrogen atmosphere at a temperate ramp rate of 20 °C/min. The glass transition and melting temperatures were determined according to the protocol in ASTM D3418-08. Tapping mode atomic force microscopy (AFM) images were obtained using a NanoScope IIIa atomic force microscope from Veeco Instruments. A Perkin-Elmer Pyris 1 TGA was used for thermal gravimetrical analysis. X-ray diffraction patterns of GO paper were collected at ambient temperature using a Rigaku R-AXIS Spider diffractometer with an imaging plate detector using graphite-monochromated Cu Kα radiation (1.5406 Å). Samples were glued to the tip of a glass capillary. Images were collected sequentially with a collection time of 2 min, and the face of the films was oriented parallel or normal to the beam. Images were integrated from 2.0° to 50° 2θ with a 0.1° step size with the AreaMax software package. Powder patterns were processed in Jade 6.5 to calculate peak positions.

The mixing enthalpy between PVA and water, RG and water, and PVA and RG was determined by a NANO ITC from TA Instruments. In a typical experiment, 50 μL of PVA was placed in the top syringe and 350 μL of 0.14 mg/mL RG was put in the bottom sample cell. After stabilization at 25 °C for about 20 min, 48 μL of PVA was injected into RG within 1 min. The released energy was obtained from integration of the exothermal peak.

The resistance of the films was measured by the four-point probe method with an Agilent 3440A multimeter. The four electrodes were made on a 3 mm by 30 mm sample strip with silver epoxy and further annealed at 70 °C for 1 h. The silver epoxy can ensure a good contact for all layers of the RG.

Uniaxial tensile testing and dynamic mechanical analysis (DMA) were done on an RSAIII Rheometrics Systems analyzer from TA Instruments. The tensile tests conform to the ASM standard ASTM D882. In a typical measurement, a 1 mm wide and 6 mm long sample strip was fixed on the steel grips either by gripping or double tape (thin films) and tested at a speed of 0.01 mm/s. In order to correctly measure the specimen extension, gauge marks were put onto the sample surface with a white marker and recorded with a high-speed camera during the testing (Figure S6a). The specimen images were then analyzed by the software to track the marks' movement to obtain the extension. Each sample was measured at least five times. In a DMA test, the sample was prestretched by 0.5%, and the experiment was run at a dynamic strain of 0.2% with a static force larger than the dynamic force by 25% from room temperature to 200 °C at a rate of 5 °C/min in air. The agreement between the storage modulus measured by DMA and Young's modulus determined by this uniaxial tensile test further validates the method in use for correctly reflecting the failure strain of samples (Table 1).

Conflict of Interest: The authors declare no competing financial interest.

Supporting Information Available: Figure S1 to S7 and theoretical calculations of Young's modulus and strength. This material is available free of charge *via* the Internet at http://pubs.acs.org.

Acknowledgment. The authors thank Dr. Antek G. Wong-Foy and Prof. Adam J. Matzger in the Department of Chemistry, University of Michigan, for the XRD analysis of samples and Dr. Kai Sun from EMAL for help with TEM imaging. The TEM sample preparation was performed in the Microscopy and Image-analysis Laboratory (MIL) at the University of Michigan, Department of Cell & Developmental Biology, with the assistance of Krystyna Pasyk and Dotty Sorenson. The MIL is a multiuser imaging facility supported by NIH-NCI, O'Brien Renal Center, UM Medical School, Endowment for the Basic Sciences (EBS), the CDB Department, and the University of Michigan. This material is based upon work partially supported by the Center for Solar and Thermal Energy Conversion, an Energy Frontier Research Center funded by the U.S. Department of Energy, Office of Science, Office of Basic Energy Sciences, under award number #DE-SC0000957. We acknowledge support from the NSF under grants ECS-0601345; EFRI-BSBA 0938019; CBET 0933384; CBET 0932823; and CBET 1036672. The work is also partially supported by AFOSR MURI 444286-P061716, the DARPA MATLOG program, and NIH 1R21CA121841-01A2. The authors thank the University of Michigan's EMAL for its assistance with electron microscopy and for the NSF grant #DMR-9871177 for funding for the JEOL 2010F analytical electron microscope used in this work.

REFERENCES AND NOTES

1. Podsiadlo, P.; Kaushik, A. K.; Arruda, E. M.; Waas, A. M.; Shim, B. S.; Xu, J. D.; Nandivada, H.; Pumplin, B. G.; Lahann, J.; Ramamoorthy, A.; *et al.* Ultrastrong and Stiff Layered Polymer Nanocomposites. *Science* **2007**, *318*, 80–83.
2. Shim, B. S.; Zhu, J.; Jan, E.; Critchley, K.; Ho, S. S.; Podsiadlo, P.; Sun, K.; Kotov, N. A. Multiparameter Structural Optimization of Single-Walled Carbon Nanotube Composites: Toward Record Strength, Stiffness, and Toughness. *ACS Nano* **2009**, *3*, 1711–1722.
3. Bonderer, L. J.; Studart, A. R.; Gauckler, L. J. Bioinspired Design and Assembly of Platelet Reinforced Polymer Films. *Science* **2008**, *319*, 1069–1073.
4. Zhu, J.; Shim, B. S.; Di Prima, M.; Kotov, N. A. Transparent Conductors from Carbon Nanotubes LbI-Assembled with Polymer Dopant with $\Pi-\Pi$ Electron Transfer. *J. Am. Chem. Soc.* **2011**, *133*, 7450–7460.
5. Walther, A.; Bjurhager, I.; Malho, J.-M.; Pere, J.; Ruokolainen, J.; Berglund, L. A.; Ikkala, O. Large-Area, Lightweight and Thick Biomimetic Composites with Superior Material Properties Via Fast, Economic, and Green Pathways. *Nano Lett.* **2010**, *10*, 2742–2748.
6. Podsiadlo, P.; Sui, L.; Elkasabi, Y.; Burgardt, P.; Lee, J.; Miryala, A.; Kusumaatmaja, W.; Carman, M. R.; Shtein, M.; Kieffer, J.; *et al.* Layer-by-Layer Assembled Films of Cellulose Nanowires with Antireflective Properties. *Langmuir* **2007**, *23*, 7901–7906.
7. Nogi, M.; Iwamoto, S.; Nakagaito, A. N.; Yano, H. Optically Transparent Nanofiber Paper. *Adv. Mater.* **2009**, *21*, 1595–1598.
8. Wu, Z. C.; Chen, Z. H.; Du, X.; Logan, J. M.; Sippel, J.; Nikolou, M.; Kamaras, K.; Reynolds, J. R.; Tanner, D. B.; Hebard, A. F.; *et al.* Transparent, Conductive Carbon Nanotube Films. *Science* **2004**, *305*, 1273–1276.
9. Zhao, X.; Zhang, Q.; Hao, Y.; Li, Y.; Fang, Y.; Chen, D. Alternate Multilayer Films of Poly(Vinyl Alcohol) and Exfoliated Graphene Oxide Fabricated Via a Facial Layer-by-Layer Assembly. *Macromolecules* **2010**, *43*, 9411–9416.
10. Putz, K. W.; Compton, O. C.; Palmeri, M. J.; Nguyen, S. T.; Brinson, L. C. High-Nanofiller-Content Graphene Oxide–Polymer Nanocomposites Via Vacuum-Assisted Self-Assembly. *Adv. Funct. Mater.* **2010**, *20*, 3322–3329.
11. Shin, M. K.; Lee, B.; Kim, S. H.; Lee, J. A.; Spinks, G. M.; Gambhir, S.; Wallace, G. G.; Kozlov, M. E.; Baughman, R. H.; Kim, S. J. Synergistic Toughening of Composite Fibres by Self-Alignment of Reduced Graphene Oxide and Carbon Nanotubes. *Nat. Commun.* **2012**, *3*, 650.
12. An, Z.; Compton, O. C.; Putz, K. W.; Brinson, L. C.; Nguyen, S. T. Bio-Inspired Borate Cross-Linking in Ultra-Stiff Graphene Oxide Thin Films. *Adv. Mater.* **2011**, *23*, 3842–3846.
13. Yang, Y.; Bolling, L.; Priolo, M. A.; Grunlan, J. C. Super Gas Barrier and Selectivity of Graphene Oxide-Polymer Multilayer Thin Films. *Adv. Mater.* **2013**, *25*, 503–508.
14. Zhu, J.; Andres, C. M.; Xu, J.; Ramamoorthy, A.; Tsotsis, T.; Kotov, N. A. Pseudonegative Thermal Expansion and the State of Water in Graphene Oxide Layered Assemblies. *ACS Nano* **2012**, *6*, 8357–8365.
15. Decher, G. Fuzzy Nanoassemblies: Toward Layered Polymeric Multicomposites. *Science* **1997**, *277*, 1232–1237.
16. Ariga, K.; Hill, J. P.; Ji, Q. Layer-by-Layer Assembly as a Versatile Bottom-up Nanofabrication Technique for Exploratory Research and Realistic Application. *Phys. Chem. Chem. Phys.* **2007**, *9*, 2319–2340.

17. Hammond, P. T. Engineering Materials Layer-by-Layer: Challenges and Opportunities in Multilayer Assembly. *AIChE J.* **2011**, *57*, 2928–2940.
18. Li, Y.-Q.; Yu, T.; Yang, T.-Y.; Zheng, L.-X.; Liao, K. Bio-Inspired Nacre-Like Composite Films Based on Graphene with Superior Mechanical, Electrical, and Biocompatible Properties. *Adv. Mater.* **2012**, *24*, 3426–3431.
19. Sen, D.; Buehler, M. J. Structural Hierarchies Define Toughness and Defect-Tolerance Despite Simple and Mechanically Inferior Brittle Building Blocks. *Sci. Rep.* **2011**, *1*, 1–9.
20. Dikin, D. A.; Stankovich, S.; Zimney, E. J.; Piner, R. D.; Dommett, G. H. B.; Evmenenko, G.; Nguyen, S. T.; Ruoff, R. S. Preparation and Characterization of Graphene Oxide Paper. *Nature* **2007**, *448*, 457–460.
21. Sriupayo, J.; Supaphol, P.; Blackwell, J.; Rujiravanit, R. Preparation and Characterization of A-Chitin Whisker-Reinforced Poly(Vinyl Alcohol) Nanocomposite Films with or without Heat Treatment. *Polymer* **2005**, *46*, 5637–5644.
22. Lee, C.; Wei, X. D.; Kysar, J. W.; Hone, J. Measurement of the Elastic Properties and Intrinsic Strength of Monolayer Graphene. *Science* **2008**, *321*, 385–388.
23. Bae, S.; Kim, H.; Lee, Y.; Xu, X. F.; Park, J. S.; Zheng, Y.; Balakrishnan, J.; Lei, T.; Kim, H. R.; Song, Y. I.; *et al.* Roll-to-Roll Production of 30-Inch Graphene Films for Transparent Electrodes. *Nat. Nanotechnol.* **2010**, *5*, 574–578.
24. Balandin, A. A.; Ghosh, S.; Bao, W. Z.; Calizo, I.; Teweldebrhan, D.; Miao, F.; Lau, C. N. Superior Thermal Conductivity of Single-Layer Graphene. *Nano Lett.* **2008**, *8*, 902–907.
25. Kulkarni, D. D.; Choi, I.; Singamaneni, S. S.; Tsukruk, V. V. Graphene Oxide−Polyelectrolyte Nanomembranes. *ACS Nano* **2010**, *4*, 4667–4676.
26. Yang, X.; Qiu, L.; Cheng, C.; Wu, Y.; Ma, Z.-F.; Li, D. Ordered Gelation of Chemically Converted Graphene for Next-Generation Electroconductive Hydrogel Films. *Angew. Chem.* **2011**, *50*, 7325–7328.
27. Putz, K. W.; Compton, O. C.; Segar, C.; An, Z.; Nguyen, S. T.; Brinson, L. C. Evolution of Order during Vacuum-Assisted Self-Assembly of Graphene Oxide Paper and Associated Polymer Nanocomposites. *ACS Nano* **2011**, *5*, 6601–6609.
28. Strawhecker, K. E.; Manias, E. Structure and Properties of Poly(Vinyl Alcohol)/Na+ Montmorillonite Nanocomposites. *Chem. Mater.* **2000**, *12*, 2943–2949.
29. Ricciardi, R.; Auriemma, F.; De Rosa, C.; Lauprêtre, F. X-Ray Diffraction Analysis of Poly(Vinyl Alcohol) Hydrogels, Obtained by Freezing and Thawing Techniques. *Macromolecules* **2004**, *37*, 1921–1927.
30. Strawhecker, K. E.; Manias, E. AFM of Poly(Vinyl Alcohol) Crystals Next to an Inorganic Surface. *Macromolecules* **2001**, *34*, 8475–8482.
31. Lee, C.; Kim, I.; Shin, H.; Kim, S.; Cho, J. Nonvolatile Resistive Switching Memory Properties of Thermally Annealed Titania Precursor/Polyelectrolyte Multilayers. *Langmuir* **2009**, *25*, 11276–11281.
32. Giri, G.; Verploegen, E.; Mannsfeld, S. C. B.; Atahan-Evrenk, S.; Kim, D. H.; Lee, S. Y.; Becerril, H. A.; Aspuru-Guzik, A.; Toney, M. F.; Bao, Z. Tuning Charge Transport in Solution-Sheared Organic Semiconductors Using Lattice Strain. *Nature* **2011**, *480*, 504–508.
33. Podsiadlo, P.; Tang, Z.; Shim, B. S.; Kotov, N. A. Counterintuitive Effect of Molecular Strength and Role of Molecular Rigidity on Mechanical Properties of Layer-by-Layer Assembled Nanocomposites. *Nano Lett.* **2007**, *7*, 1224–1231.
34. Ramanathan, T.; Abdala, A. A.; Stankovich, S.; Dikin, D. A.; Herrera Alonso, M.; Piner, R. D.; Adamson, D. H.; Schniepp, H. C.; Chen, X.; Ruoff, R. S.; *et al.* Functionalized Graphene Sheets for Polymer Nanocomposites. *Nat. Nanotechnol.* **2008**, *3*, 327–331.
35. Debenedetti, P. G.; Stillinger, F. H. Supercooled Liquids and the Glass Transition. *Nature* **2001**, *410*, 259–267.
36. Anastasiadis, S. H.; Karatasos, K.; Vlachos, G.; Manias, E.; Giannelis, E. P. Nanoscopic-Confinement Effects on Local Dynamics. *Phys. Rev. Lett.* **2000**, *84*, 915–918.
37. Jackson, A. P.; Vincent, J. F. V.; Turner, R. M. The Mechanical Design of Nacre. *Proc. R. Soc. B* **1988**, *234*, 415–440.
38. Padawer, G. E.; Beecher, N. On the Strength and Stiffness of Planar Reinforced Plastic Resins. *Polym. Eng. Sci.* **1970**, *10*, 185–192.
39. van Es, M. A. *Polymer-Clay Nanocomposites: The Importance of Particle Dimensions*. Ph.D. thesis, University of Delft, 2001.
40. Liang, J.; Huang, Y.; Zhang, L.; Wang, Y.; Ma, Y.; Guo, T.; Chen, Y. Molecular-Level Dispersion of Graphene into Poly(Vinyl Alcohol) and Effective Reinforcement of Their Nanocomposites. *Adv. Funct. Mater.* **2009**, *19*, 2297–2302.
41. Ritchie, R. O. The Conflicts between Strength and Toughness. *Nat. Mater.* **2011**, *10*, 817–822.
42. Launey, M. E.; Ritchie, R. O. On the Fracture Toughness of Advanced Materials. *Adv. Mater.* **2009**, *21*, 2103–2110.
43. Chen, H.; Muller, M. B.; Gilmore, K. J.; Wallace, G. G.; Li, D. Mechanically Strong, Electrically Conductive, and Biocompatible Graphene Paper. *Adv. Mater.* **2008**, *20*, 3557–3561.
44. Stankovich, S.; Dikin, D. A.; Dommett, G. H. B.; Kohlhaas, K. M.; Zimney, E. J.; Stach, E. A.; Piner, R. D.; Nguyen, S. T.; Ruoff, R. S. Graphene-Based Composite Materials. *Nature* **2006**, *442*, 282–286.
45. Bai, Y.; Ho, S.; Kotov, N. A. Direct-Write Maskless Lithography of LBL Nanocomposite Films and Its Prospects for MEMS Technologies. *Nanoscale* **2012**, *4*, 4393–4398.
46. Jiang, C. Y.; Markutsya, S.; Pikus, Y.; Tsukruk, V. V. Freely Suspended Nanocomposite Membranes as Highly Sensitive Sensors. *Nat. Mater.* **2004**, *3*, 721–728.
47. Shutava, T. G.; Balkundi, S. S.; Vangala, P.; Steffan, J. J.; Bigelow, R. L.; Cardelli, J. A.; O'Neal, D. P.; Lvov, Y. M. Layer-by-Layer-Coated Gelatin Nanoparticles as a Vehicle for Delivery of Natural Polyphenols. *ACS Nano* **2009**, *3*, 1877–1885.
48. Zhang, H.; Shih, J.; Zhu, J.; Kotov, N. A. Layered Nanocomposites from Gold Nanoparticles for Neural Prosthetic Devices. *Nano Lett.* **2012**, *12*, 3391–3398.
49. Schaaf, P.; Voegel, J.-C.; Jierry, L.; Boulmedais, F. Spray-Assisted Polyelectrolyte Multilayer Buildup: From Step-by-Step to Single-Step Polyelectrolyte Film Constructions. *Adv. Mater.* **2012**, *24*, 1001–1016.
50. Hummers, W. S.; Offeman, R. E. Preparation of Graphitic Oxide. *J. Am. Chem. Soc.* **1958**, *80*, 1339–1339.
51. Li, D.; Muller, M. B.; Gilje, S.; Kaner, R. B.; Wallace, G. G. Processable Aqueous Dispersions of Graphene Nanosheets. *Nat. Nanotechnol.* **2008**, *3*, 101–105.